energies

MDPI

Article

Impacts of Different Operation Conditions and Geological Formation Characteristics on CO_2 Sequestration in Citronelle Dome, Alabama

Ebrahim Fathi [1], Danilo Arcentales [2,*] and Fatemeh Belyadi [3]

[1] Department of Petroleum and Natural Gas Engineering, West Virginia University, Morgantown, WV 26506, USA
[2] Escuela Superior Politécnica del Litoral, ESPOL, Facultad de Ingeniería en Ciencias de la Tierra, Campus Gustavo Galindo Km. 30.5 Vía Perimetral, Guayaquil P.O. Box 09-01-5863, Ecuador
[3] Obsertelligence LLC, Aubrey, TX 76227, USA
* Correspondence: daanarce@espol.edu.ec

Abstract: Major concerns of carbon dioxide (CO_2) sequestration in subsurface formations are knowledge of the well injectivity and gas storage capacity of the formation, the CO_2 pressure and saturation plume extensions during and after injection, and the risks associated with CO_2 leakage and fault reactivation. Saline reservoirs are considered as one of the target formations for CO_2 sequestration through structural, residual, dissolution, and mineral trapping mechanisms. The boundary condition of the saline reservoir dictates the pressure and saturation plume extension of the injected supercritical CO_2 that could expand over large distances. This can lead to sources of risk, e.g., leakage and/or fault reactivation due to presence of wells, thief zones, and geological discontinuities. Therefore, there is a critical need to develop a model that describes how risk-related performance metrics (i.e., the CO_2 saturation plume size, the pressure differential plume area, and the pressure differential at specific locations) vary as a function of the size of injection, time following injection, injection operations, and geologic environment. In this study, a systematic reservoir modeling studies of anthropogenic CO_2 sequestration in Citronelle dome, Alabama, was performed where all relevant scenarios and conditions to address the questions of the saturation and pressure plume size in the area of review (AoR) and post-injection site care (PISC) are considered. The objective for this study was firstly to systematically simulate CO_2 sequestration, i.e., saturation dynamics, and pressure behavior over a range of operational and geological conditions and to derive conclusions about the factors influencing saturation and pressure plume size, post-injection behavior, and the risk associated with them, by developing third-generation reduced order models (ROMs) for reservoir behavior. Finally, to assess the uncertainty associated with our studies, Latin Hypercube Sampling (LHS) together with an experimental design technique, i.e., Plackett–Burman design, was used. Application of Pareto charts and respond surfaces enabled us to determine the most important parameters impacting saturation and pressure plume sizes and to quantify the auto- and cross-correlation among different parameters in both history-matched and upscaled models.

Keywords: CO_2 sequestration; pressure and saturation dynamics; reduced order model; Citronelle

Citation: Fathi, E.; Arcentales, D.; Belyadi, F. Impacts of Different Operation Conditions and Geological Formation Characteristics on CO_2 Sequestration in Citronelle Dome, Alabama. *Energies* **2023**, *16*, 3191. https://doi.org/10.3390/en16073191

Academic Editor: Mehrdad Massoudi

Received: 25 February 2023
Revised: 24 March 2023
Accepted: 25 March 2023
Published: 1 April 2023

1. Introduction

Massive quantities of anthropogenic carbon dioxide (CO_2) emissions from different fossil fuels have been identified as the main driving mechanism of climate change and global warming. By the end of 2021, more than 81% of primary energy in the USA came from fossil fuels, of which more than 60% was used for electricity generation. Coal combustion, which was the most carbon-intensive source of electricity generation in the world by more than 15 billion tons of CO_2 emissions in 2021, provides more than 21% of the USA's electricity and more than 74% and 63% of India's and China's electricity, respectively (U.S.

Energy Information Administration, Monthly Energy Review, Table 1.3 and 10.1, April 2022). Other source of carbon emissions, such as oil, gas flaring, and cement production, also play significant roles in CO_2 emission. Carbon Capture Utilization and Storage (CCUS) is recognized as one of the advanced technologies to mitigate climate change by capturing and storing CO_2 in underground natural reservoirs [1]. Depleted oil and gas reservoirs are considered as storage sites with a significant potential to store carbon dioxide, as they stored hydrocarbons for millions of years. One of the most important aspects of CO_2 storage in depleted oil and gas reservoirs is the availability of the infrastructure required for the storage, such as equipment and pipelines, which significantly helps the economics of the carbon storage project. The oil and gas industries historically used the carbon captured for both enhanced oil and gas recovery, through injection into semi-depleted reservoirs [2–4]. However, the problem of early CO_2 breakthrough from producing wells, rock and fluid interactions, and failures in long-term reservoir integrity due to presence of multiple adjacent operating wells, limited its application, which requires detailed studies on field stress correlation with CO_2 injection [5]. The application of CO_2-enhanced shale gas recovery was also studied experimentally [6], where gas storage capacity of shale was compared using multiple gases. The numerical simulation of CO_2-enhanced shale gas recovery also showed great promise for CO_2 sequestration and enhanced shale gas recovery [7,8]. Among different CO_2 storage sites, saline reservoirs were found to be more promising for sequestering large amounts of carbon dioxide [9]. Different techniques have also been used to enhance CO_2 storage in saline aquifers, such as water alternate gas (WAG) injection and brine extraction in Minnelusa sandstone [10] or CO_2 storage in deep offshore saline aquifers [11]. Ref. [12] compared the storage capacity of depleted gas reservoirs and aquifers and found that even though the aquifers have much lower compressibility, due to their far larger extent they offer immense potential for CO_2 storage. In this case, the CO_2–brine interaction played a significant role in the success of the CO_2 storage project. There are multiple trapping mechanisms that can facilitate the process of CO_2 storage in underground formations, including structural, residual, solubility, and mineral trapping. The structural trapping mechanism is the most common among these, where the low permeability formation confines the reservoir and acts as a seal that prevents CO_2 migration to the surface due to buoyancy effect. The residual trapping mechanism is where the injected CO_2 becomes trapped as discrete droplets due to the surface tension. This trapping mechanism works best from a retention perspective since the trapped gas will not move or be displaced [13]. Solubility trapping occurs when the injected CO_2 becomes dissolved in formation water, developing a denser fluid that sinks and helps to increase the storage capacity of the formation. Bennion et al. 2008 [14], showed that the solubility of CO_2 in brine has a direct relationship with pressure and as reservoir pressure increases due to the CO_2 injection, higher CO_2 solubility in brine is achieved. They also showed that CO_2 solubility and CO_2–brine interfacial tension decreases as salinity increases. Mineral trapping, even though it is a slower process, is considered as the safest process that occurs due to chemical reactions between injected CO_2 and formation minerals, resulting in different carbonate precipitations. In every CO_2 storage process one or multiple forms of trapping mechanism might be involved. In this study, carbon storage in an aquifer, the Citronelle saline reservoir, was used for the systematical analysis of the impacts of different operation conditions and geological formation characteristics on area of review (AoR), post-injection site care (PISC) and risk associated with anthropogenic CO_2 sequestration. The manuscript is structured as follows: the field background was studied first; then the numerical reservoir model was developed, history-matched and upscaled; next the sensitivity and uncertainty analyses were performed using Latin Hypercube Sampling, and results are discussed in detail for both AoR and PISC metrics; and finally, the influence of different reservoir and operational parameters on performance metrics was studied using statistical analysis.

Citronelle Field Background

The Citronelle CO_2 storage project was developed in the Citronelle dome north of Mobile County, AL, USA, and is used for multiple large-capacity CO_2 sequestration projects. The Citronelle is an elliptical structural closure free of any major faulting zones. Existing seismic data in the southeast Citronelle field were studied to corroborate this structure at the planned injection test location. Sonic logs were used to link the reflectors obtained from two linear seismic reflection arrays running from north to south and from northeast to southwest, of stratigraphic units. Existing seismic reflection data analysis indicated that the top of the Paluxy formation is considered a strong reflector unbroken by faults. Moreover, sand layers inside the Paluxy were imaged to be laterally continuous for substantial distances [15]. As of December 2019, up to 100,000 tons of CO_2 has been captured from the coal-fired power generation facility "Power plant Barry" and stored in the storage site via twelve miles of pipeline (i.e., injection well D-9-7 located in the southeast Unit). Figure 1 shows the location of the Citronelle field and the carbon capture facility. The Citronelle oil field was discovered in 1955. In the first 10 years of discovery, 434 productive wells were drilled, of which 139 were utilized for improved oil recovery using water flooding [16]. Currently, the Citronelle operator unit demonstrates safe and secure CO_2 injection and storage in extensive saline reservoirs. The geology of the Citronelle is described as the Paluxy formation located at depths of 9400 to 10,500 feet (TVD) and consists of 1100 feet of sandstone inter-bedded with siltstone and shale. This formation is separated by two extensive shale layers from the Washita Fredericksburg sand (saline reservoir) at the top and the Donovan sand (oil reservoir) at the bottom. According to previous studies made in this field, 17 sand layers were detected and correlated using petro-physical logs and core data [17]. In addition to the Upper Tuscaloosa Formation, this deep saline reservoir contains multiple geologic confining units that serve as a barrier enclosure to prevent leakage of CO_2 to the surface. The Massive and Pilot sands of the lower Tuscaloosa Group, as well as several sandstone units in the upper Tuscaloosa Group and Eutaw Formation, provide potential carbon storage sites. These sandstone units have the remarkable characteristic of having high porosity and permeability and low heterogeneity. Sixteen well logs in three cross-sections (A-A′, B-B′, and C-C′) were used to interpret the structure of the Paluxy formation (Figure 2). The Paluxy formation, selected as the injection area, has three distinct subdivisions, including the Lower Paluxy section that has thick sandstones with interbedded shale from 10,300 to 10,500 feet, the Middle Paluxy interval composed primarily of shale and thin sandstones from 9800 to 10,300 feet, and the upper Paluxy, consisting of individual sandstones with irregular bottom sand surfaces that are characteristic of fluvial sand deposits that result from infilling of erosional topography by aggradation from 9400 to 9800 feet [4,15]. The stratigraphic column of southwest Alabama is presented in Figure 3 [18]. After distinguishing the three cross-sections, the sand correlations were mapped to assess their individual continuity. The overall thickness of these sand layers was approximately 470 feet; 17 sand layers were selected for injection based on thickness and their extension. Approximately 385 feet of the thickness were being represented by these selected layers (Figure 4). X-ray diffraction (XRD), and thin section studies were performed on the samples obtained from the injection well D-9-7. The upper Paluxy sandstone included 78% to 90% by weight quartz, 1% to 7% feldspar and 7% to 12% clay minerals. The typical upper Paluxy thin sections were also in agreement with XRD studies showing more than 50% of clay minerals to be kaolinite; they also showed moderate-to-large intergranular pores with limited secondary dissolution porosities. The grain-to-grain contacts also indicated significant compaction. (SECARB Anthropogenic Test Project Assessment Report SP121013).

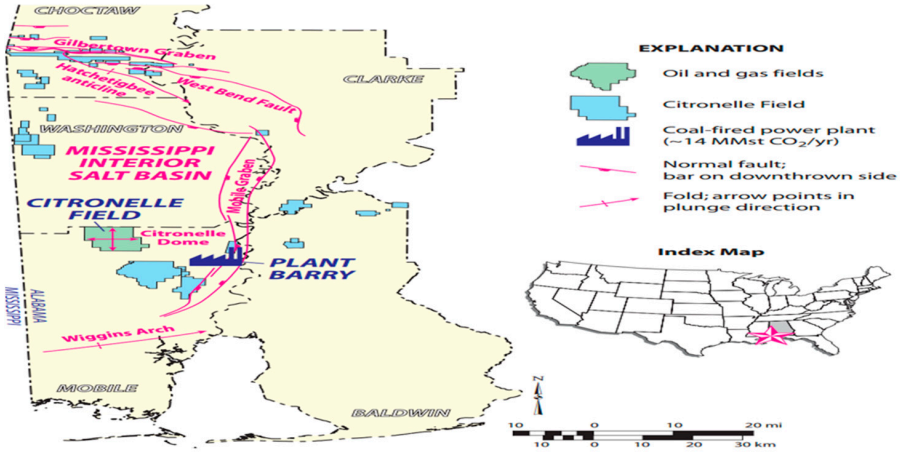

Figure 1. Location of Citronelle Field.

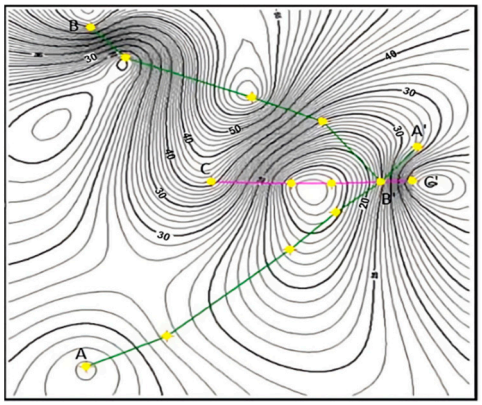

Figure 2. Cross sections in well D-9-7.

System	Series	Stratigraphic Unit	Major Sub Units	Potential Reservoirs and Confining Zones
Tertiary	Plio-Pliocene		Citronelle Formation	Freshwater Aquifer
	Miocene	Undifferentiated		Freshwater Aquifer
	Oligocene		Chicasawhay Fm.	Base of USDW
		Vicksburg Group	Bucatunna Clay	Local Confining Unit
	Eocene	Jackson Group		Minor Saline Reservoir
		Claiborne Group	Talahatta Fm.	Saline Reservoir
	Paleocene	Wilcox Group	Hatchetigbee Sand Bashi Marl Salt Mountain LS	Saline Reservoir
		Midway Group	Porters Creek Clay	Confining Unit
Cretaceous	Upper	Selma Group		Confining Unit
		Eutaw Formation		Minor Saline Reservoir
		Tuscaloosa Group	Upper Tusc.	Minor Saline Reservoir
			Mid. Tusc. Marine Shale	Confining Unit
			Lower Tusc. Pilot Sand Massive sand	Saline Reservoir
Cretaceous	Lower	Washita-Fredericksburg	Dantzler sand Basal Shale	Saline Reservoir Primary Confining Unit
		Paluxy Formation	'Upper' 'Middle' 'Lower'	Proposed Injection Zone
		Mooringsport Formation		Confining Unit
		Ferry Lake Anhydrite		Confining Unit
		Donovan Sand	Rodessa Fm. 'Upper' 'Middle' 'Lower'	Oil Reservoir Minor Saline Reservoir Oil Reservoir

Figure 3. Stratigraphic column for southwest Alabama.

Sand Layer	Sand Layer Top and Bottom (feet below sea-level)	Thickness (feet)
9420	9,414 – 9,421	6
9430	9,427 – 9,438	12
9460	9,444 – 9,476	32
9520	9,513 - 9,528	15
9540	9,534 - 9,549	15
9570	9,562 - 9,584	22
9620	9,596 - 9,638	42
9670	9,660 - 9,679	19
9710	9,695 - 9,717	22
9740	9,730 - 9,748	18
9800	9,775 - 9,806	30
9840	9,833 - 9,843	10
9870	9,868 - 9,874	6
9900	9,886 - 9,903	18
9940	9,929 - 9,939	10
9970	9,954 - 9,977	24
10030	10,016 - 10,025	9
10040	10,037 - 10,049	11
10060	10,055 - 10,069	15
10100	10,099 - 10,113	15
10130	10,121 - 10,134	13
10230	10,223 - 10,231	7
10310	10,302 - 10,318	16
10370	10,362 - 10,381	20
10400	10,396 - 10,412	16
10470	10,454 -10,484	31
10500	10,491 - 10,508	18

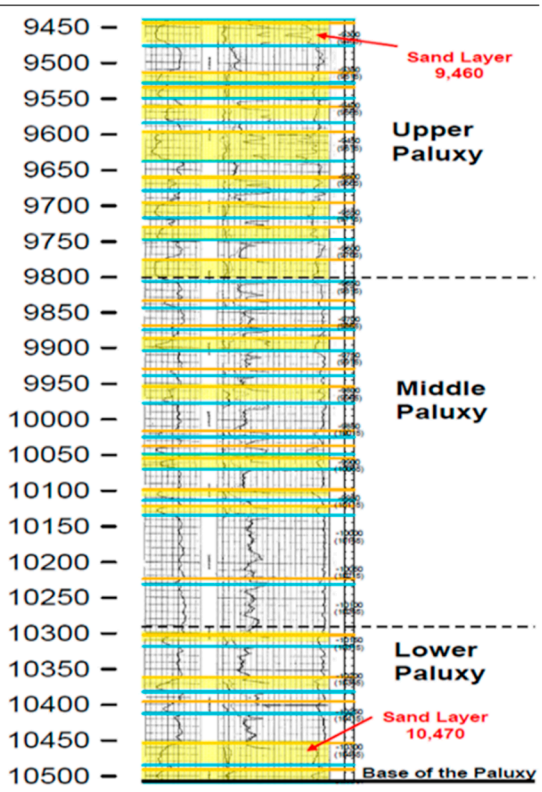

Figure 4. Individual sandstone layers selected in well D-9-7.

2. Developing an Outline for an AoR and PISC Calculation Tool

One of the main objectives of this project was to have an advance understanding of dynamics of pressure and saturation plume size in a deep saline reservoir as a function of operational and geological conditions. Careful considerations needed to be taken due to two main risks associated with storing carbon dioxide in deep saline reservoir, i.e., groundwater contamination and seismicity induced by the injection of CO_2. In aiming to characterize the reservoir behavior over time, three main metrics were identified and quantified, including pressure differential plume area, CO_2 plume area, and pressure differential at a specific location away from the injection well. These metrics will be discussed in the following sections. Figure 5 shows the schematic of the methodology applied to two reservoir models built for this study, including the history-matched model covering 5×5 km^2 area with 796,875 grids and the upscaled model covering 10×10 km^2 area with 1,437,500 grids.

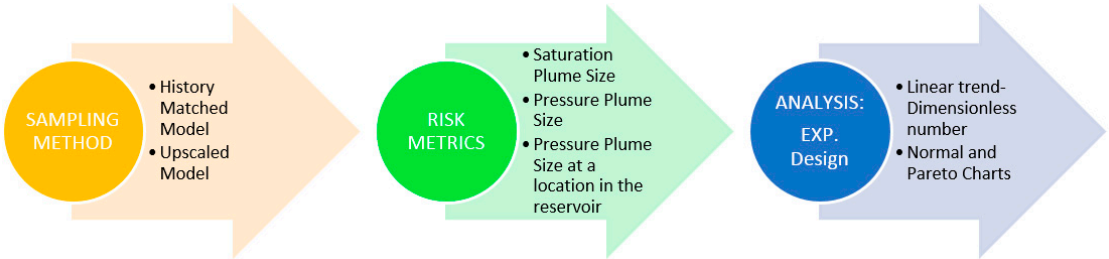

Figure 5. Methodology Flowchart.

2.1. Citronelle Numerical Model

The compositional reservoir simulation model CMG-GEM capable of simulating the multiphase, multi-component fluid flow was employed to describe the CO_2 injection into the Paluxy formation. CMG-GEM is a compositional reservoir flow model that can be used to model CO_2 trapping by pore volume, CO_2 dissolution and mineralization. Moreno

2013 performed detailed analysis of trapping mechanisms in Citronelle and showed that structural and residual trapping are more important trapping mechanisms than solubility trapping, and mineral trapping mechanism is minimal for different sets of relative permeability curves. This simulator could also track the saturation, composition, phase behavior, and permeability change as a function of pressure. Reservoir rock, fluid, and their interactions; geomechanics (dilation); well configuration, and operational condition were incorporated in this model. Seventeen sand layers were detected and correlated using petro-physical logs and core data representing 51 simulation layers. Rock properties, including porosity and permeability of Upper, Middle, and Lower Paluxy formation, were obtained using both core sample measurements and well logs. The core permeability values were log-normally distributed and ranged from 0.1 to 3950 millidarcys. The log-normal mean core permeability was 85.2 millidarcys. A range of porosity values were seen for different part of the field. The southeast side of the field showed the greatest porosity range of 21–25% while the northern part of the field showed 11–15% porosity. The Upper Paluxy formation showed 16–24% porosity and the Lower Paluxy formation showed 14–16%. The core analysis also provided the capillary pressure, relative permeability (CO_2–brine permeability) and permeability anisotropy. The reservoir pressure was continuously monitored using three observation wells equipped with downhole pressure gauges with 0.5 to 1 min time intervals. The maximum bottom-hole pressure was fixed as 6300 psi. This ensured that the formation was not going to be fractured during the injection of CO_2.

2.1.1. History-Matched Model

To discretize the structure of the Paluxy formation, a Cartesian grid system was used where first the "history-matched model" was generated with a total of 796,875 grid blocks, i.e., 125 × 125 × 51 grid in i, j, and k directions, which covered 25 square kilometers. This model included laterally discontinuous low-permeability units distributed vertically within the reservoir. For each layer porosity and permeability maps were generated as shown in Figure 6. Porosity and permeability in this reservoir were between 3–33% and 1–2100 mD, respectively. This multi-layer sandstone reservoir was modelled using both semi-open and closed boundary conditions. The injection rate was used as the constraint and field pressure was history matched.

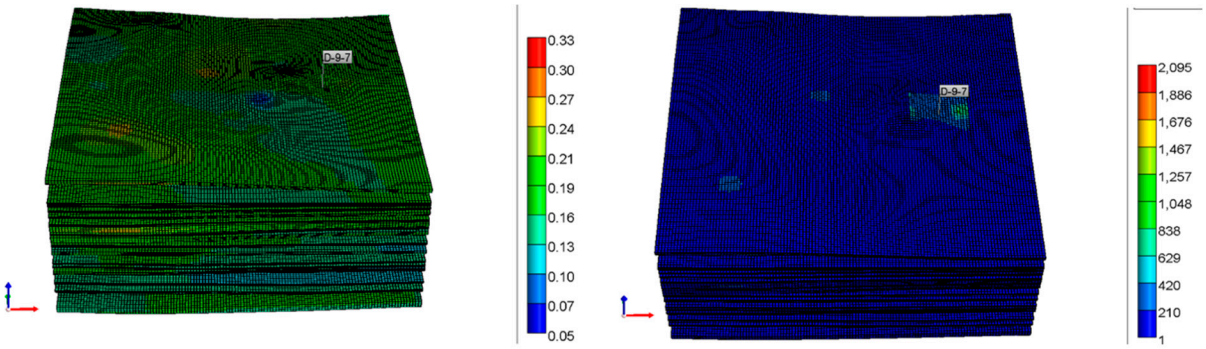

Figure 6. Porosity (**left**) and Permeability (**right**) distribution.

2.1.2. History-Matched Upscaled Model

An upscaled model of the Citronelle reservoir was built based on Cartesian grids with a total of 1,437,500 grid blocks, i.e., 250 × 250 × 23 grids in *i*, *j*, and *k* directions covering an area of 100 square kilometers using power law. Power law is one of the common techniques valid for spatial averaging in Darcy flow regimes [19]. It is defined in Equation (1) as follows:

$$\bar{F} = \left(\frac{1}{V} \int F(x)^i dV \right)^{\frac{1}{i}} \quad (1)$$

where V is the block volume and i is the power exponent ranging between -1 and 1. F is the feature to be upscaled and $\bar{F}$ is the upscaled feature in x domain.

In this enlarged model, the isopach, porosity and permeability maps were upscaled without destroying the structure of the formation. Figure 7 shows the grid top map and permeability distributions in cross-section of the upscaled model. The permeability range varied between 1 and 1000 mD, while the porosity kept the same range as the history-matched model. Compressibility of the rock varied between 1.01×10^{-5} and 1.06×10^{-6} 1/psi. The injection rate varied in a range between 10 kt/year to 5 Mt/year while injection time was fixed to 3 and 30 years. Post-injection time was also set to 50 years for 3 years of injection, and 300 years for 30 years of CO_2 injection period.

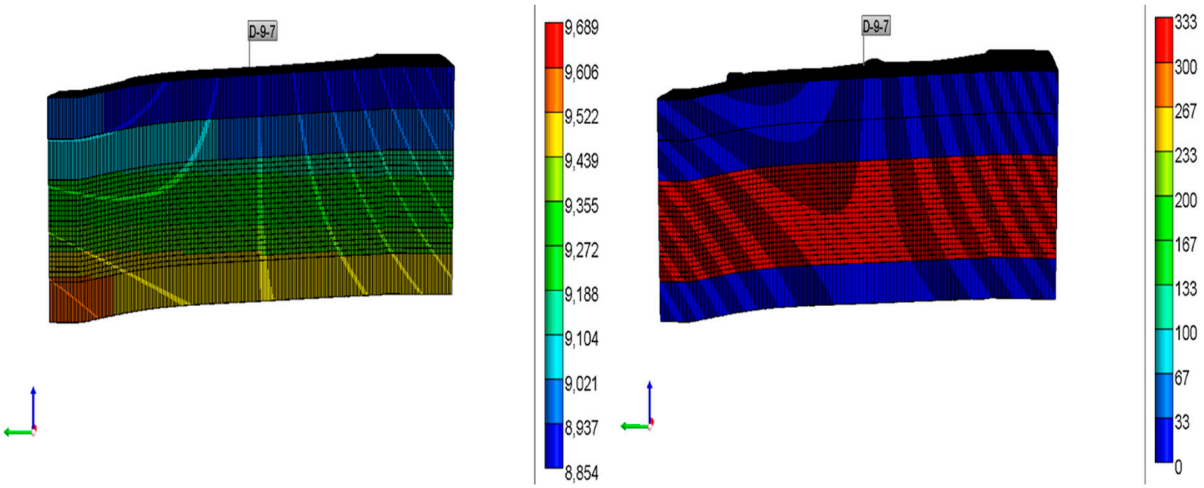

Figure 7. Grid top map (**left**) and permeability distribution (**right**) for the upscaled model.

In general, a simulation plan was generated for a better understanding of the relationship between geological/operational parameters and risk metrics implied. An overall range of simulation cases is shown in Table 1. The reservoir heterogeneity is included in permeability, porosity, compressibility and anisotropy, different relative permeability curves based on variation in residual gas, and liquid saturations generated based on experimental CO_2–brine relative permeability. To properly sample the multi-dimensional model variable space, the Latin Hypercube Sampling (LHS) method was used to generate a simulation matrix for the history-matched and the upscaled models. LHS was performed based on a statistical distribution of different model variables. The simulation responses of this study are also listed in Table 2. Thirty-five simulations were performed using the history-matched model with closed and semi-open boundary condition as illustrated in Table 3. For uncertainty quantification, more than 200 simulation runs were performed for a closed and semi-open system with 3 and 30 years of CO_2 injection using the upscaled model. For each realization, the pressure plume size and CO_2 plume size were calculated based on three pressure thresholds: 1, 5, and 10 bar, and two saturation threshold values of 1% and 20%.

Table 1. Parameter space.

Parameter Space									
Models Used	**Horizontal Size of Model Domain**	**Injection Rate**	**Injection/Post-Injection Length**	**Boundary Condition (BC)**	**Porosity**	**Compressibility**	**Dipping Angle**	**Anisotropy Ratio (kv/kh)**	**Salinity**
History-matched model; Upscaled model	10 km × 10 km; 5 km × 5 km	50, 250, 1000, 5000, kt/year	3 and 30 years injection; 30 and 300 years post injection	Closed boundary; Semi-open boundary	3–33%	1.01×10^{-5}–1.06×10^{-6} 1/psi	Structural map	0.01–1	10–230 g/L

Table 2. Simulation response.

1- Area of review (AoR)	2- Post-injection site care (PISC)
(a) Maximum CO_2 saturation at any time during injection	(a) For 3 years of injection: 50 years of post-injection
(b) Maximum pressure increase	(b) For 30 years of injection: 300 years of post-injection

Table 3. Performance metrics for H-M model.

#RUNS	Injection Length (yr.)	Injection Rate (kt/yr.)	Post-Injection Length (yr.)	Model Domain Size (km × km)	Reservoir Thickness (m)	Permeability (md)	Porosity	Compressibility (1/psi)	Boundary Type
1	30	5000	300	5 × 5	Maps	Maps	Maps	3×10^{-6}	Closed
2	3	250	50	5 × 5	Maps	Maps	Maps	1×10^{-6}	Closed
3	30	5000	300	5 × 5	Maps	Maps	Maps	9×10^{-6}	Closed
4	30	1000	50	5 × 5	Maps	Maps	Maps	9×10^{-6}	Closed
5	3	250	300	5 × 5	Maps	Maps	Maps	3×10^{-6}	Closed
6	30	5000	300	5 × 5	Maps	Maps	Maps	1×10^{-6}	Closed
7	30	5000	50	5 × 5	Maps	Maps	Maps	9×10^{-6}	Closed
8	30	5000	50	5 × 5	Maps	Maps	Maps	3×10^{-6}	Closed
9	30	10	50	5 × 5	Maps	Maps	Maps	1×10^{-6}	Closed
10	30	5000	50	5 × 5	Maps	Maps	Maps	1×10^{-6}	Closed
11	3	1000	50	5 × 5	Maps	Maps	Maps	9×10^{-6}	Closed
12	3	5000	300	5 × 5	Maps	Maps	Maps	3×10^{-6}	Closed
13	3	250	50	5 × 5	Maps	Maps	Maps	1×10^{-6}	Closed
14	3	250	300	5 × 5	Maps	Maps	Maps	1×10^{-6}	Closed
15	30	5000	300	5 × 5	Maps	Maps	Maps	1×10^{-6}	Closed
16	3	50	300	5 × 5	Maps	Maps	Maps	9×10^{-6}	Closed
17	3	250	50	5 × 5	Maps	Maps	Maps	3×10^{-6}	Closed
18	3	5000	300	5 × 5	Maps	Maps	Maps	3×10^{-6}	Closed
19	3	250	50	5 × 5	Maps	Maps	Maps	3×10^{-6}	Closed
20	3	5000	300	5 × 5	Maps	Maps	Maps	1×10^{-6}	Closed
21	3	1000	50	5 × 5	Maps	Maps	Maps	9×10^{-6}	Closed
22	30	1000	50	5 × 5	Maps	Maps	Maps	1×10^{-6}	Closed
23	3	50	50	5 × 5	Maps	Maps	Maps	1×10^{-6}	Closed
24	3	1000	300	5 × 5	Maps	Maps	Maps	3×10^{-6}	Closed
25	30	10	50	5 × 5	Maps	Maps	Maps	3×10^{-6}	Closed
26	30	1000	50	5 × 5	Maps	Maps	Maps	3×10^{-6}	Closed
27	30	250	300	5 × 5	Maps	Maps	Maps	9×10^{-6}	Closed
28	3	10	300	5 × 5	Maps	Maps	Maps	3×10^{-6}	Closed
29	3	10	300	5 × 5	Maps	Maps	Maps	1×10^{-6}	Closed

3. Results (Site-Specific Application of AoR and PISC Tool)

In this section, pressure expansion and CO_2 plume size during injection and post injection was investigated. For the purpose, three metrics were identified to evaluate and analyze the reservoir behavior during injection and post injection, including the CO_2 plume area (saturation plume size), the pressure differential plume area, and the pressure differential at specific locations in the reservoir. Figures 8 and 9 show the CO_2 saturation and pressure distributions at the end of 3 and 30 years of CO_2 injection in the upscaled Citronelle reservoir. Different thresholds were assigned to pressure and saturation to study the CO_2 plume size and pressure area, i.e., 1, 5 and 10 bar for pressure and 0.01 and 0.2 for CO_2 saturation. For each pressure and saturation threshold, the plume size and pressure area were obtained from simulation results of CMG-GEM using an in-house program

developed by Seth King at the National Energy Technology Laboratory (NETL); results were then compared and used toward the study of the reservoir fluid dynamics behavior.

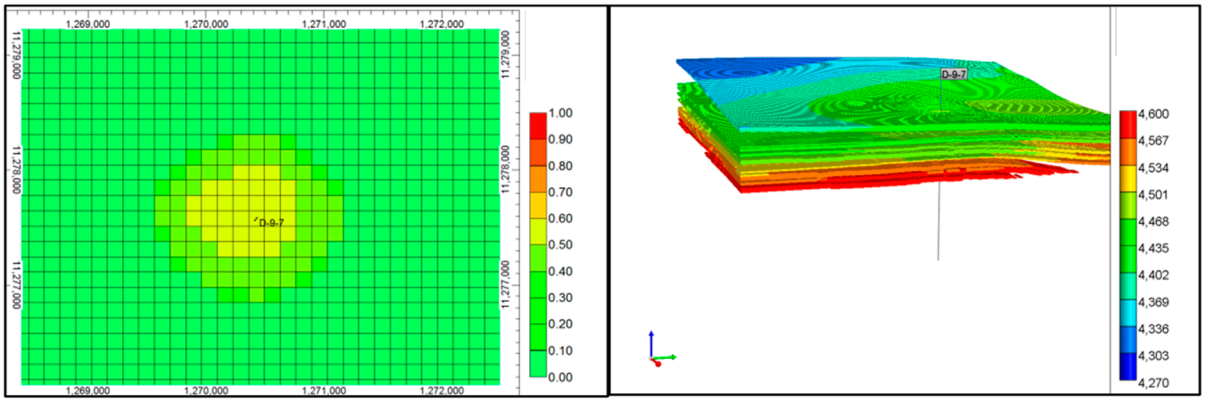

Figure 8. CO_2 saturation distribution (**left**) and pressure distribution (**right**) at the end of 3 years of injection for the history-matched model.

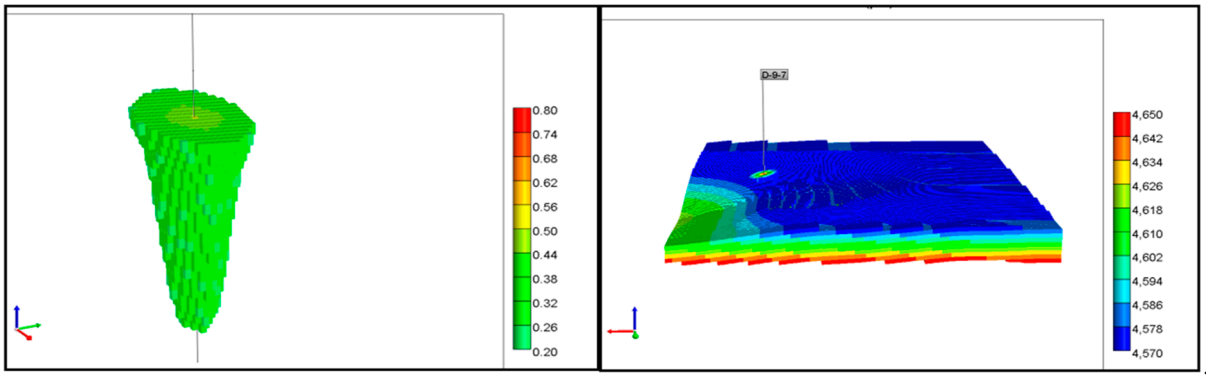

Figure 9. CO_2 saturation distribution (**left**) and pressure distribution (**right**) at the end of 30 years of injection for the upscaled matched model.

Different boundary conditions can impact the rate and magnitude of pressure and saturation change in the reservoir. Here, to investigate the impact of using different boundary conditions on simulation responses and to study the possibility of having significant impact of boundary condition on uncertainty analysis, we introduced the closed and semi-open boundary conditions as new variables in our study for the history-matched model and compared the simulation responses and uncertainty analysis of these two cases. A closed system with a no-flow boundary was defined by setting an impermeable barrier as a cap rock at the north boundary and setting a low-perm layer at the top of the south boundary. For the semi-open system, we performed the same north and south impermeable boundaries; however, a flow boundary condition was applied by setting an aquifer surrounding the storage site (Figure 10). Saturation and pressure plume sizes were used as simulation responses for both semi-open and closed systems.

3.1. CO_2 Saturation Plume

The current analysis tracked for this first metric was based on the evolution of the saturation plume size over time while injecting and for post-injection, which would help us to determine how site risks behaved over time. Figure 11 shows a schematic that describes the behavior of saturation plume size over time. The plume size expanded fast during the injection period (early phase), and then slowed down after injection ended (long-term phase). Even though plumes did not always have a roundabout shape, they were assumed as such when aiming to derive the radius of the plume from the calculated plume area. The

growth rate of plume size expansion at early and late times could be characterized with the slopes of m_1 and m_2.

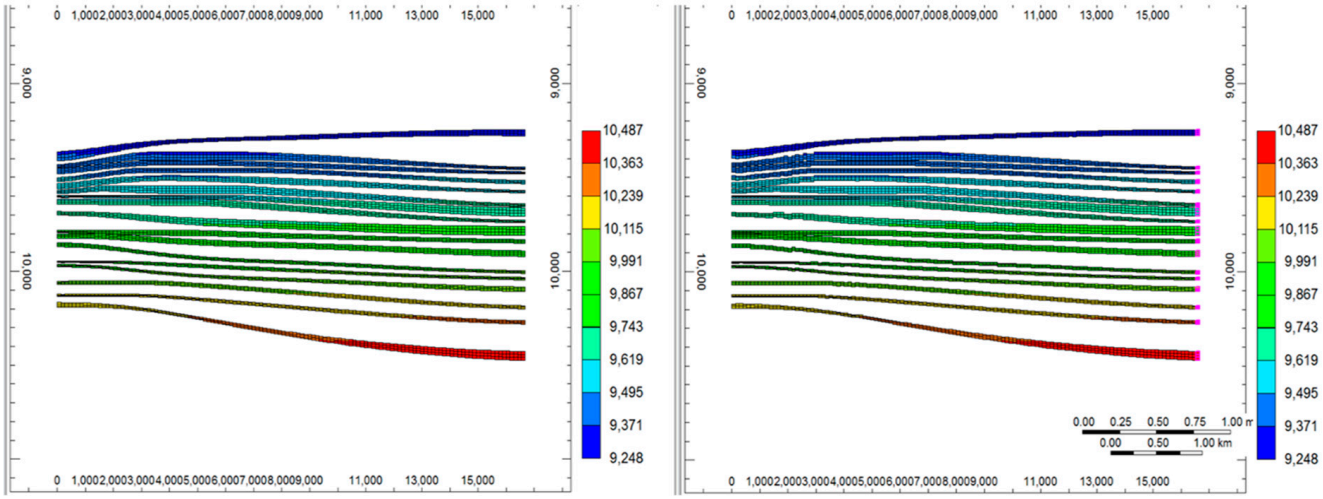

Figure 10. Cross-section view of no-flow boundary (**left**) and semi-open boundary (**right**).

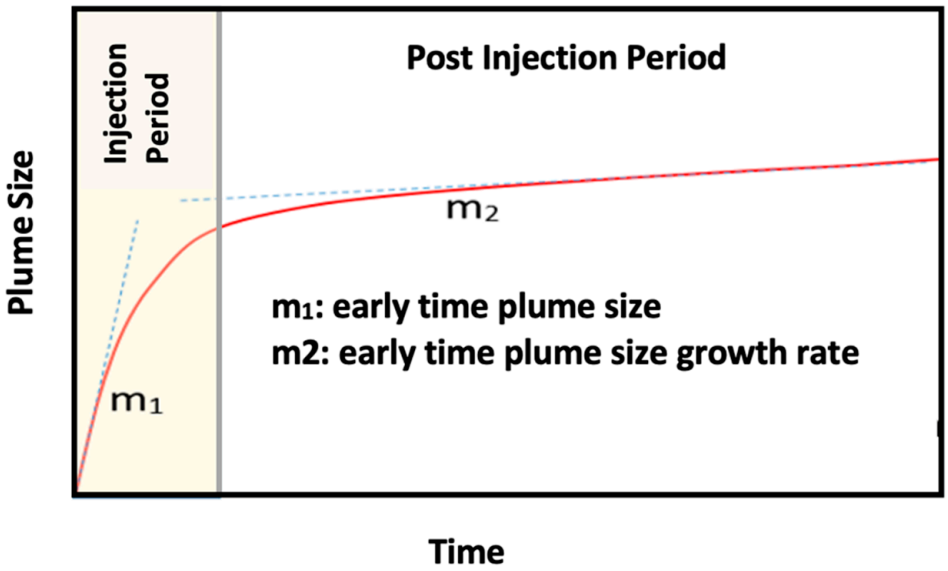

Figure 11. Time evolution of CO_2 saturation plume size.

3.2. Area of Pressure Plume

Similar to saturation plume size, pressure plume size was also studied using multiple pressure thresholds. Based on a class V permit obtained in 2012, the AoR was defined as the region surrounding the injection point where the pressure will see a 2 percent increase compared to its native pressure. As detailed in the schematic (Figure 12a), the pressure plume size showed a different profile in comparison with the CO_2 saturation plume; the pressure plume size started increasing at the beginning of the injection until it reached its highest point, usually sometime after injection ended. Then, the plume size started decreasing at different rates depending on the boundary condition applied (closed or semi-open). Figure 12b shows the behavior of the pressure plume in the case of the closed boundary condition. The effective radius of the pressure plume was obtained by assuming a circular shape of the plume area.

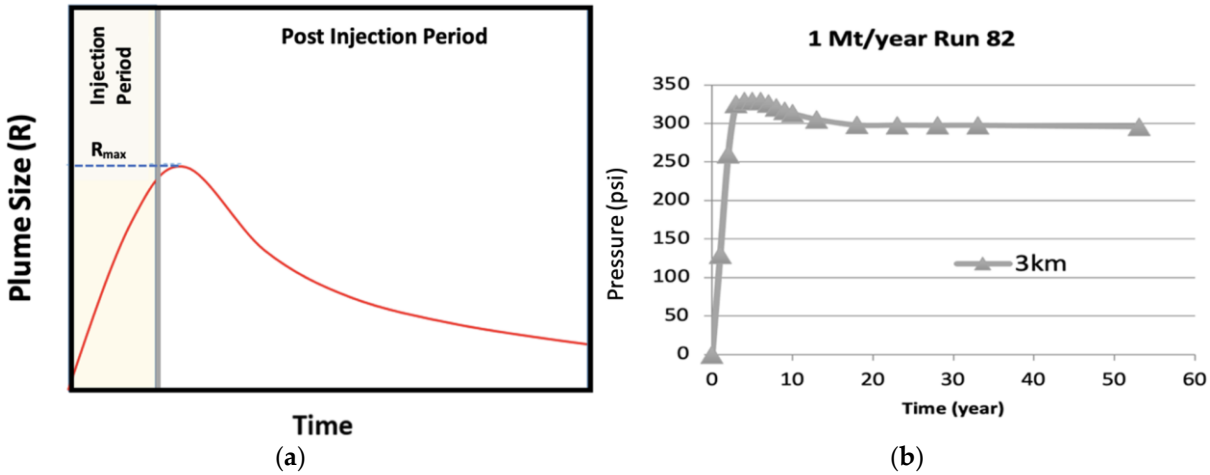

(**a**) (**b**)

Figure 12. (**a**) Schematic of usual pressure plume behavior. (**b**) Time evolution of pressure plume size for a specific threshold for a closed boundary condition.

3.3. Pressure at a Location in the Reservoir

Finally, the pressure plume size was analyzed at various distances from the injection point including 1, 2 and 3 km. Figure 13a shows the schematic of pressure dynamics at a specific location away from the injection point. The pressure profile shows a rapid increase during injection that reached its maximum pressure at the end of injection period. After injection stopped the pressure started decaying. The rate of pressure decay was related to the specific boundary condition applied. The maximum pressure at a specific location was reached at the end of injection or sometime after injection stopped, depending on the distance from the injection point and reservoir heterogeneity. It is important to note that the pressure differential was calculated assuming the reservoir was in hydrostatic equilibrium before injection started. Figure 13b shows the time evolution of pressure at 1 km away from injection point assuming 50 kt/year of injection.

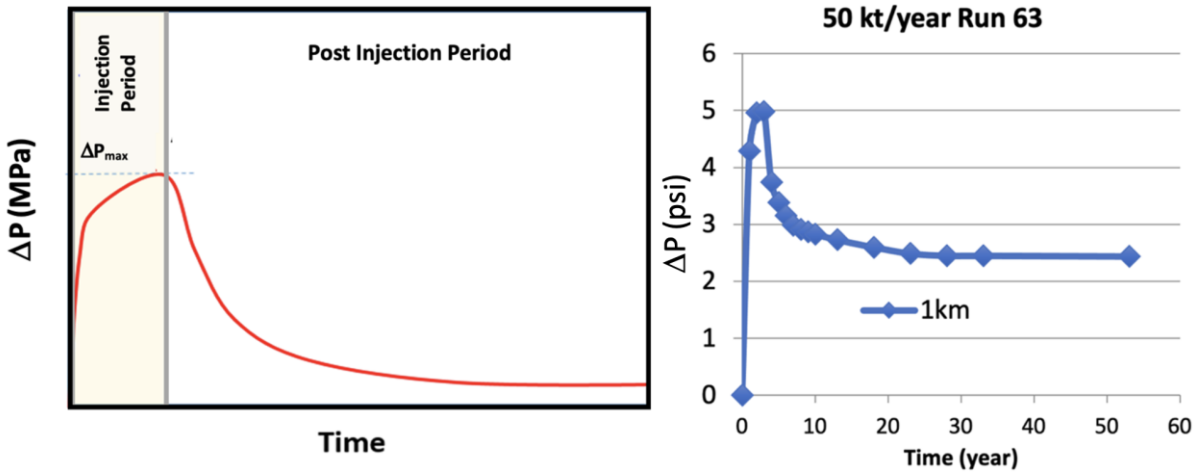

(**a**) (**b**)

Figure 13. (**a**) Schematic of time evolution of pressure at a particular point in reservoir. (**b**) Time evolution of pressure at 1 km away from injection point assuming 50 kt/year of injection.

An analysis of how pressure changed after 1 year of injection and fifty years of post-injection was performed by investigating the dynamics of pressure build-ups at 1 kilometer away from the injection point where the injection rate was changing from 50 kilotons per year to 3.5 million tons per year. Comparing all different cases, we can clearly see that the pressure increased rapidly and then suddenly declined after shutting in the injector well.

However, the pressure stabilization was reached almost 20 years after the injection stopped (Figure 14). The same trend was observed when the pressure build-up was investigated at 2 and 3 kilometers away from the injection point.

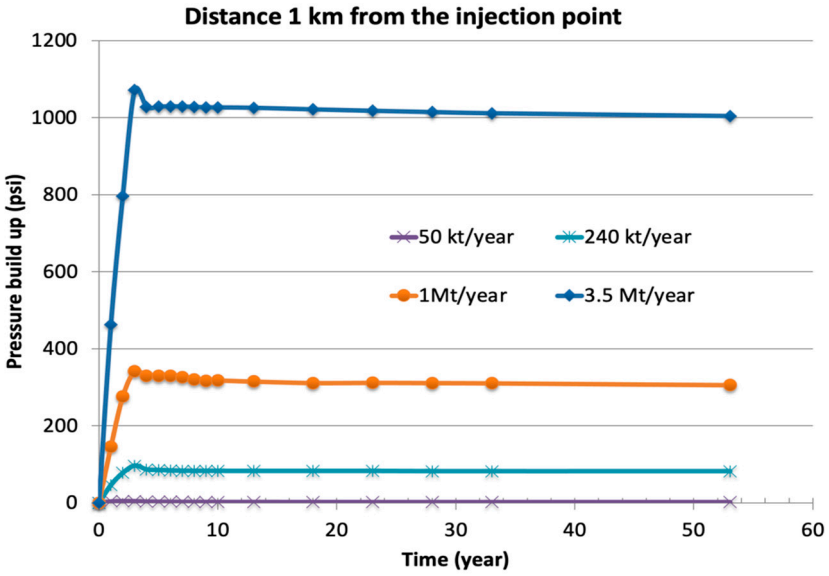

Figure 14. Pressure build-up vs. time at 1km away from injection point for a closed boundary aquifer system.

4. Discussion (Detailed Analysis of Reservoir Behavior)

A systematic approach was implemented to perform the sensitivity analysis for both reservoir models, i.e., history-matched and upscaled models, to find the most important parameters impacting the saturation and pressure plume size. This included determining the parameters of interests, performing a screening analysis to find the "heavy hitters" using Plackett–Burman (PB) analysis, performing comprehensive analysis to understand the non-linear behavior of important parameters, and finally generating the response surfaces.

4.1. Analysis of Results

The conventional approach to studying the simulation results is to use cross-plot analysis where the pressure and saturation plume size are plotted against injection rate. Here, the expectation is to see larger areal plume expansion by increasing the injection rate; however, since the problem involves multi-variables with non-linear special and temporal correlations the simulation response might not be intuitive. Therefore, we have used a dimensionless number to be able to characterize this complex fluid dynamics problem using a reduced order model. A dimensionless number represents the overall impact of different variables and their correlations to simulation response, i.e., saturation and pressure plume size. For the purpose, a dimensionless number "Ψ" is defined in Equation (2) including the most important parameters obtained from experimental design analysis.

$$\Psi = \frac{q \times t}{\emptyset \times \rho \times h \times \log(k)} \tag{2}$$

where: q = injection rate (kt/years); t = injection length (year); $\emptyset$ = porosity (dimensionless); ρ = CO_2 density (kt/m^3); h = thickness (m); k = permeability (m^2).

Figures 15 and 16 show the simulation response vs. dimensionless number for two cases of closed and semi-open boundary conditions. There is a clear linear trend observed when saturation plume size is plotted against the dimensionless number. A similar linear trend between pressure plume size and dimensionless number is also obtained and illustrated in Figure 16. In the case of pressure plume size, unlike saturation plume size,

different critical values are obtained for different pressure threshold values above which the pressure plume reaches the boundary of the reservoir.

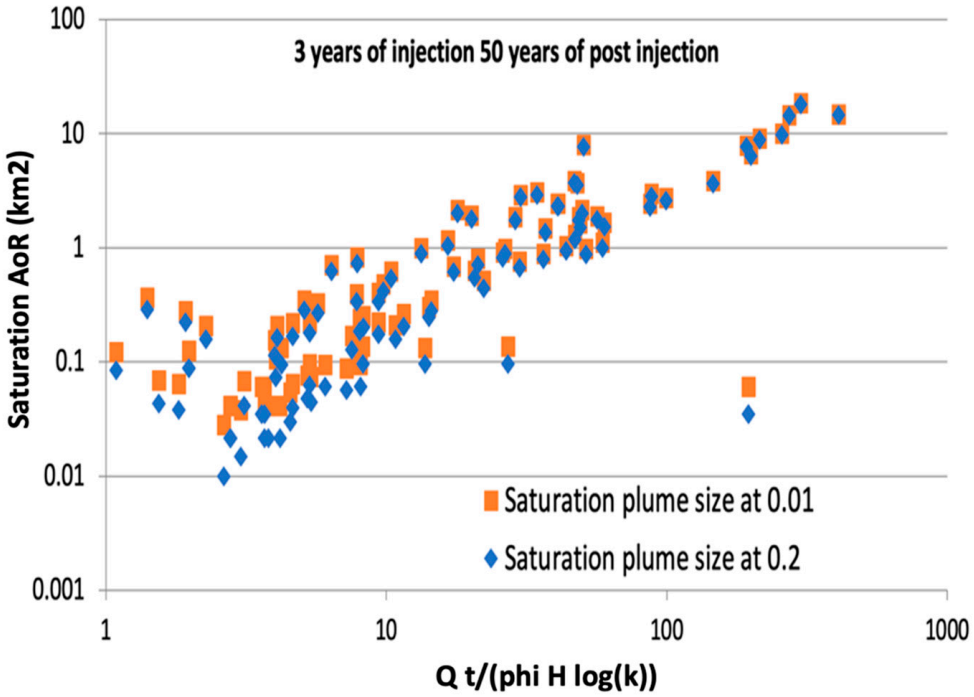

Figure 15. Saturation plume size vs. dimensionless number using upscaled model for semi-open system.

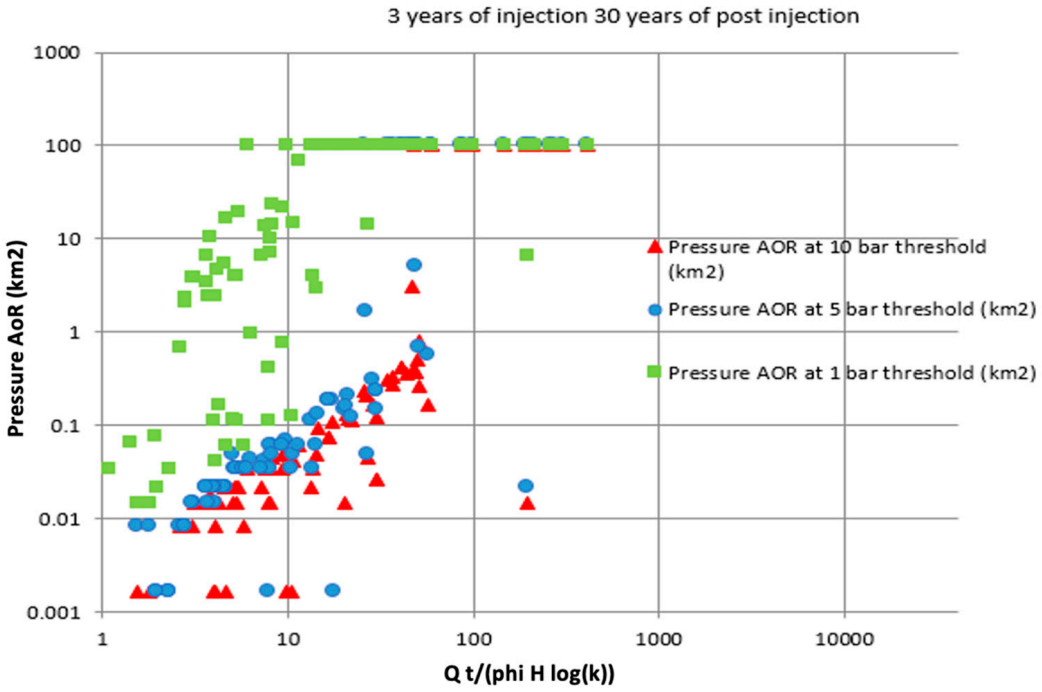

Figure 16. Pressure plume size vs. dimensionless number using upscaled model for closed system.

Sensitivity analyses were performed to see the impacts of different parameters on the dimensionless number Ψ as shown in Figure 17. The effect of a combination of different parameters on the dimensionless number were studied by varying the parameters of interest and keeping the rest constant. Saturation AoR showed the highest sensitivity to a combination of permeability, thickness, and injection rate and the lowest sensitivity to a combination of porosity, permeability, and injection rate.

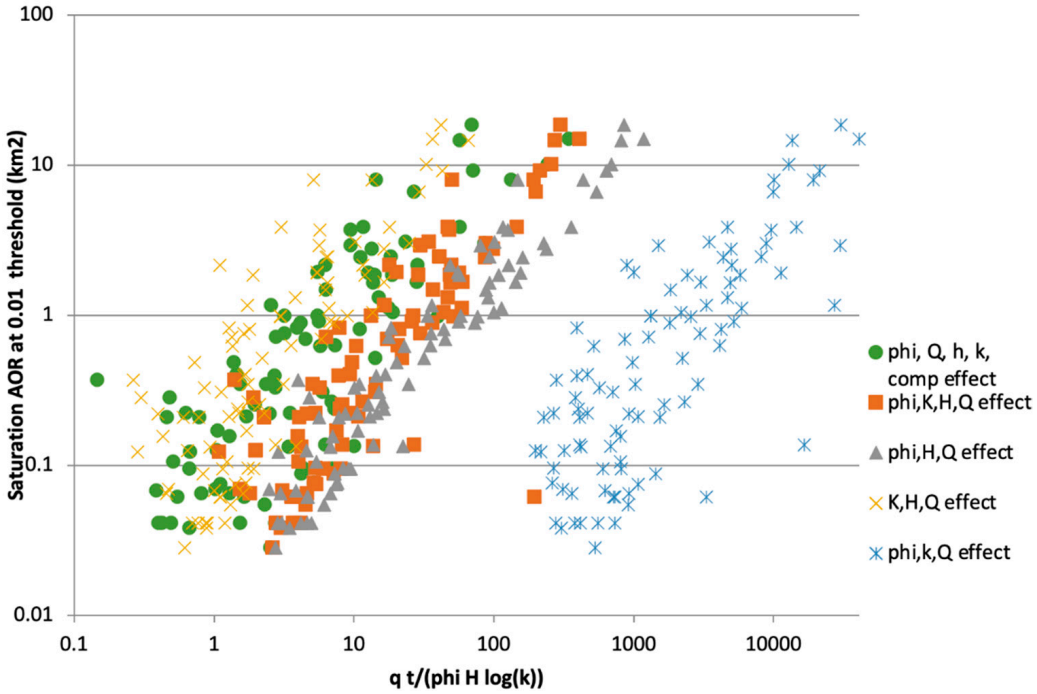

Figure 17. Linear relationship between different components of dimensionless number and risk metrics.

4.2. Plackett–Burman Design

Systematic approach was used for both reservoir models to find the most important parameters affecting the dynamics of CO_2 saturation and pressure plume size. This included determining the parameters of interest, performing a screening analysis to find the "heavy hitters" using Plackett–Burman, and performing a comprehensive analysis to understand the non-linear behavior of important parameters using both history-matched and upscaled models. Plackett–Burman (PB) design, as used here, is the most compact two-level design that requires $(n + 1)$ runs, where n is the number of factors or variables. In PB design, all the columns of the design matrix are orthogonal to each other and can analyze all the main effects. Table 4 shows the seven parameters selected and their level of variation. Tables 4 and 5 show the terminology of a two-level design matrix for history-matched and upscaled models where the highest value for the factors is represented with (+1), and the low values with (−1). In this study, saturation and pressure plume size have been used as the simulation response.

Table 4. Parameter setting of PB design.

Parameter	−1	+1	Unit
A: Permeability	10.19	977.22	Md
B: kv/kh	0.0106	0.9947	NA
C: Porosity	0.0501	0.3478	%
D: Thickness	50	200	m
E: Compressibility	1.06×10^{-6}	1.01×10^{-5}	1/psi
F: Salinity	11.37	228.12	ppm
G: Injection rate	20	4274	kt/year

Table 5. PB design for seven variables, −1 = low value, +1 = high value, 12 realizations.

	Factor 1	Factor 2	Factor 3	Factor 4	Factor 5	Factor 6	Factor 7
RUN	**A: Permeability**	**B: kv/kh**	**C: Porosity**	**D: Thickness**	**E: Compressibility**	**F: Salinity**	**G: Injection Rate**
	md	NA	%	m	1/psi	ppm	kt/year
1	−1	1	1	−1	1	−1	−1
2	−1	−1	1	1	1	−1	1
3	−1	1	1	1	−1	1	1
4	1	−1	−1	−1	1	1	1
5	1	1	−1	1	−1	−1	−1
6	−1	−1	−1	−1	−1	−1	−1
7	1	1	1	−1	1	1	−1
8	1	−1	1	−1	−1	−1	1
9	−1	1	−1	−1	−1	1	1
10	1	1	−1	1	1	−1	1
11	1	−1	1	1	−1	1	−1
12	−1	−1	−1	1	1	1	−1

4.3. Pareto and Normal Plot Charts

In this study, the Pareto chart, the normal plot of the standardized effects and 3D surface responses were used for the analysis. The Pareto chart displays the relative size of the effects and present the contribution of the simulation response, i.e., pressure and saturation plume size. It uses dimensionless statistics to scale the effects in terms of standard deviations. These are *t*-values obtained from a *t*-test and *p*-values using statistical significance. In this design, the Pareto chart analyzes the uncertainty into three different classes. The variable has with certainty a significant impact in simulation response if it falls above a line defined based on confidence intervals and has no significant impact on simulation results if it falls below the line. From the following Pareto charts, Figures 18–20, reservoir permeability and injection rate obtained had considerable influence on the pressure and saturation plume size for all the thresholds and boundary conditions. Figure 18 shows that the main parameters impacting the size of a CO_2 saturation plume were reservoir permeability, injection rate, porosity, and compressibility; these are showing a higher impact on the simulation response. However, salinity, reservoir anisotropy and thickness show minimal impact. In the normal probability plot of the effects, points that do not fall near the red line usually indicate important effects. Important effects are larger and further from the fitted line than unimportant effects. Unimportant effects tend to be smaller and centered on zero. Additionally, the normal plot can tell the effect polarity of each variable. For example, in Figure 18, the standard effect of reservoir permeability is positive, which means that in a higher permeability reservoir, the saturation plume expands faster. Normal plots also show that reservoir permeability, injection rate, and compressibility have a positive correlation with saturation size whereas porosity has a negative correlation.

Similar analysis was performed using pressure plume size as a simulation response, with 1, 5 and 10 bar pressure thresholds. Figure 19 summarizes the Pareto and normal plot analysis for pressure plume size with different pressure thresholds. At a small pressure increase with a threshold of 1 bar injection rate, reservoir thickness and porosity showed significant impact on pressure plume size, while at higher pressure thresholds of 5 and 10 bar injection rates, reservoir permeability consistently showed a profound impact on the size of the pressure plume.

As discussed earlier, Plackett–Burman design is a two-level design. To break down the aliasing in a two-level design a standard method is to use the fold-over technique. Typically, the fold-over is performed by simply changing the signs of all the columns in the design of the experiment in Table 5. Full fold-over significantly increases the resolution of the results.

Figure 20 shows the Pareto chart obtained from analysis of a fully fold-over PB design that agrees with our previous observations and shows the robustness of the calculations.

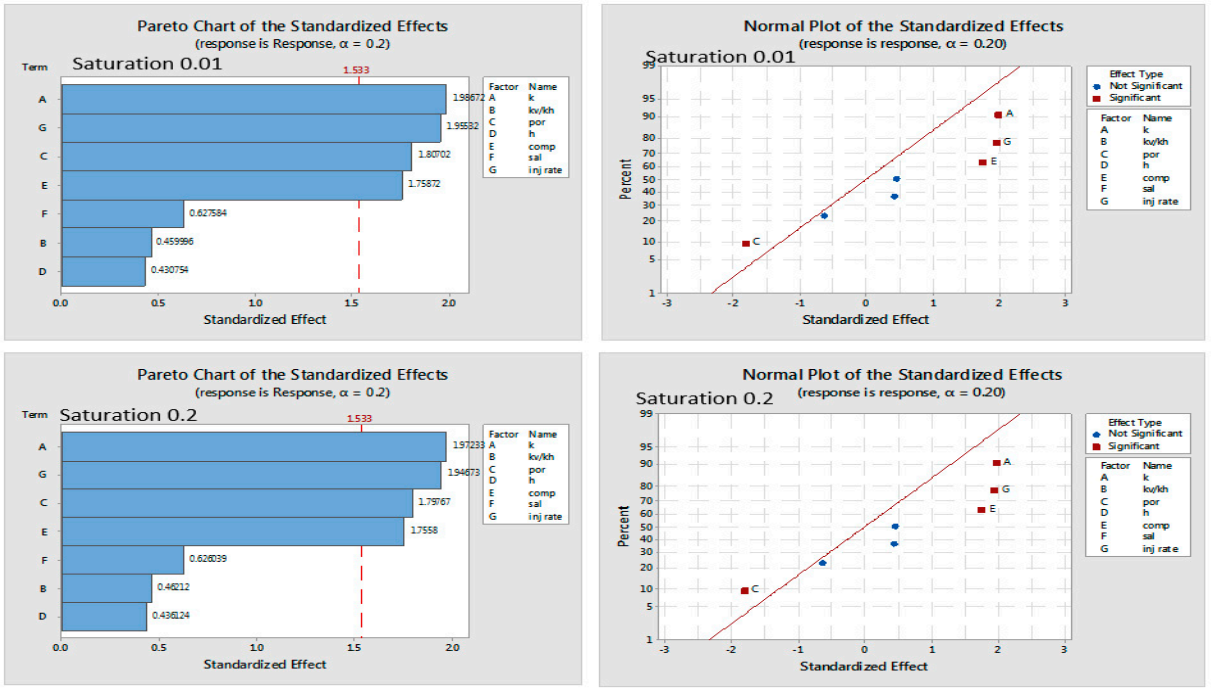

Figure 18. Pareto and Normal plot charts of upscaled model using saturation plume size for closed system.

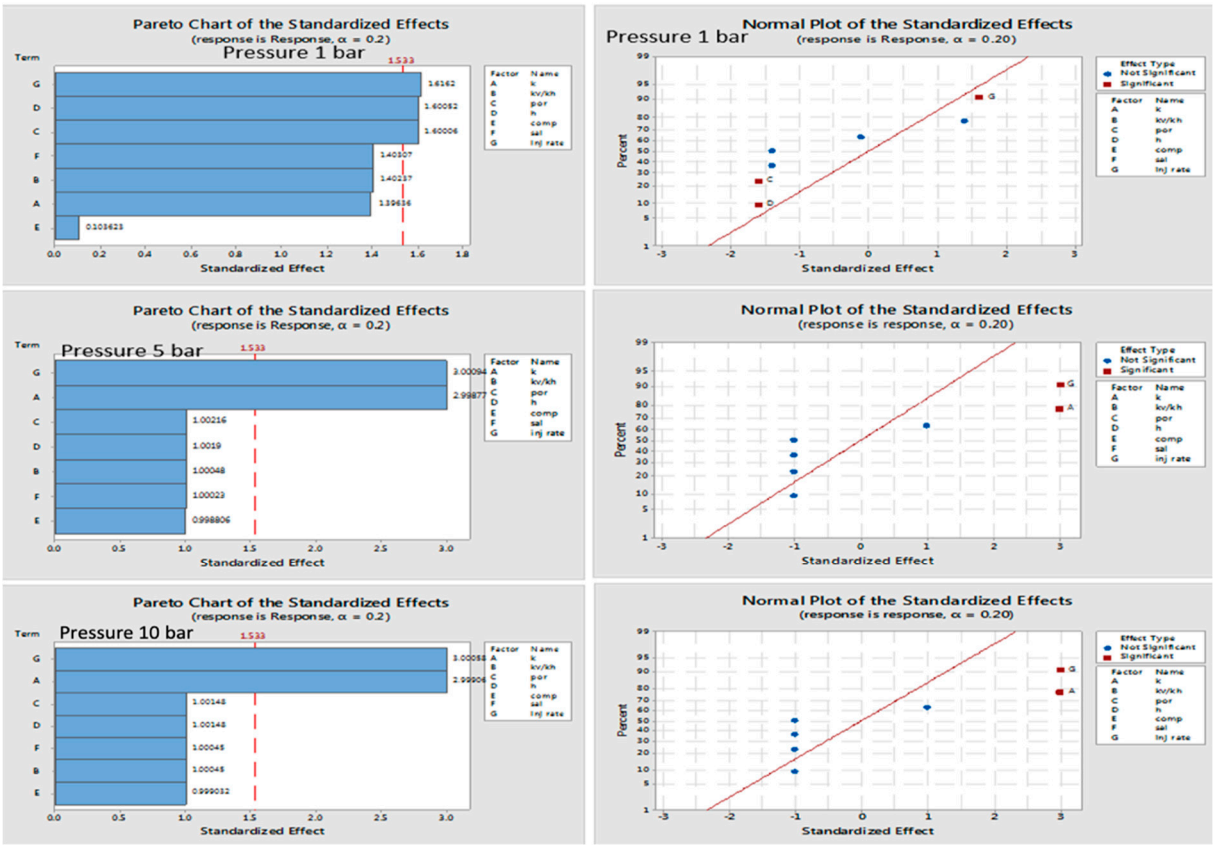

Figure 19. Pareto and Normal plot charts of upscaled model using pressure plume size for closed system.

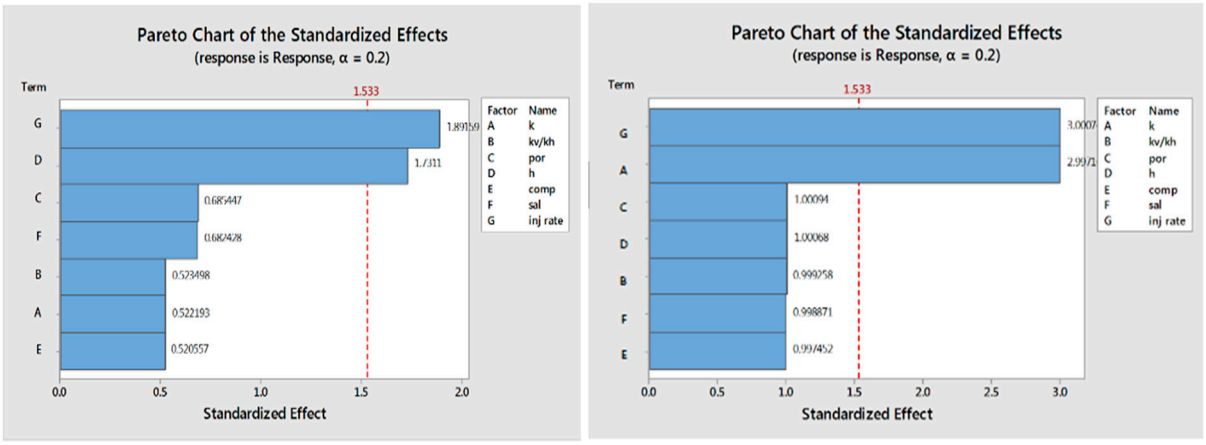

Figure 20. Pareto charts of upscaled model using pressure plume size for 1 and 5 bar of thresholds.

4.4. Response Surface

Response surfaces are usually used to explore the relationships between significant parameters obtained through application of Pareto charts and a simulation response, i.e., saturation and pressure plume size in this study. Surface responses can also be used as a proxy to the system or as an optimization strategy. In reservoir simulation studies, developing a relationship between porosity, permeability, and reservoir response usually attracts huge interest. Figure 21 shows the surface responses developed to find the regression between porosity, permeability, and pressure plume size with different pressure thresholds using the upscaled model with closed boundary condition. For more detailed studies, a few exploratory runs were performed to validate the accuracy of the surface responses and regressions generated between porosity, permeability, and pressure plume size.

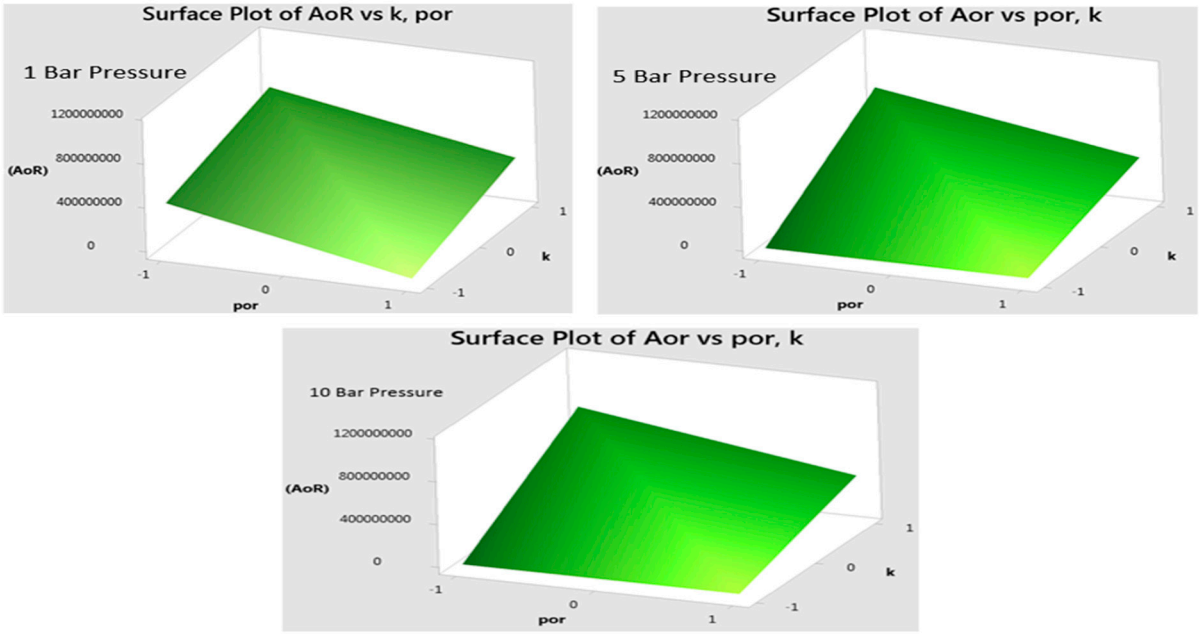

Figure 21. Surface plots of AoR vs. porosity and permeability for different pressure and saturation thresholds for upscaled model.

4.5. Qualitative Assessment

In this study we focused on three aspects of reservoir performance regarding CO_2 injection and used these as risk matrices, including the CO_2 plume area, the pressure differential plume area, and the pressure differential at a point. This helped us to understand the

relationship between the size and duration of injection with AoR and PISC and how this would impact the risk associated with the injection. The evaluation of pressure differential and CO_2 plume extension can be used to identify any risk associated with CO_2 leakage to possible ground waters or reaching to critical pressure for fault or fracture reactivation that could pose risks associated with seismicity or CO_2 leakage through faults and natural fracture systems. Even though we were not directly quantifying risks associated with CO_2 injection during and after injection stops, this aspect of reservoir behavior is central to the assessment of risk at a storage site.

After analyzing the results using sensitivity analysis, the qualitative assessment of the impacts of different geological characteristics on pressure extension and plume saturation were made and are summarized in Table 6.

Table 6. Qualitative Assessment for parameters used.

Parameter	Impact on Pressure	Impact on Saturation	Notes
Porosity	Medium	High	For closed systems, the impact of porosity can be higher, depending on pressure threshold and injection rate.
Permeability (k)	High	High	For closed systems, the impact of permeability can be lower, depending on pressure threshold and injection rate.
Compressibility	Low-Medium	Low	Compressibility will have a higher impact on pressure for a closed system where the pore volume is within an order of magnitude of the injected volume.
Thickness	Low-Medium	Low-Medium	There is some variability between reservoirs on whether thickness impacts pressure or saturation plume size more.
k_h:k_v	Low	Low-Medium	
Salinity	Low	Low	
Caprock Permeability	Low-Medium	Low	Caprock permeability has more impact when injection rate or mass is not too high and caprock permeability is low.
Boundary Conditions	Medium-High	Low	Boundary conditions are important for higher injection volumes or smaller reservoirs.

5. Conclusions

CO_2 storage in deep saline reservoirs requires an advanced understanding of reservoir rock and fluid properties, interactions, and impact of different geological and operational conditions on fluid dynamics during and after injection of anthropogenic carbon dioxide in the reservoir. This can be summarized in two underlying questions:

1. How does a reservoir's performance change as a function of injection volumes and rates of CO_2?
2. How does a reservoir behave after CO_2 injection stops as a function of time?

To answer these questions, a series of simulation runs were performed on a wide range of geological and operational conditions following a statistical approach that ensured the correct sampling of the multi-dimensional space of the model variables. The simulation results of the two models were compared and a number of differences in the impacts of reservoir parameters on saturation and pressure plume size were observed. In both the history-matched and upscaled models considering the open boundary condition, CO_2 dissolution in brine appeared as the main trapping mechanism, while in the closed boundary condition structural trapping and compaction was dominant. These two different trapping mechanisms resulted in differences in the magnitude of the impact of reservoir parameters

on both pressure and saturation plume extensions. In both cases, the CO_2 plume expanded during the injection period, and it stabilized in a slower growth rate after injection. The growth rate stoppage after injection depended on multiple geological and operational conditions and their correlations. The plume degradation stop after injection could last a few years depending on the amount of CO_2 injected and the porosity, permeability, and boundary condition of the formation. Injection rate, reservoir permeability, and boundary condition show higher impacts on saturation and pressure plume size. In open boundary cases, higher brine salinity resulted in lower CO_2 dissolution in brine and, as a result, lower impact on both saturation plume extension and differential pressure extension compared to the closed boundary condition. In closed boundary conditions, higher sand layer thickness and permeability anisotropy had less impact on saturation plume extension than in open boundary scenarios due to the higher influence of the buoyancy effect and the structure of the closed boundary reservoir. The pressure plume size depicted a rapid increase during injection in both models until it reached its maximum value before it began to decrease after injection stopped. The pressure plume size of the specific points near the injection well showed a fast increase during the injection and a rapid decrease after injection stopped. In the case of the open boundary condition, higher permeability resulted in decreasing the size of the differential pressure plume, while in the closed boundary case it resulted in increasing the differential pressure plume due to confinement.

Qualitative assessment of the geological and operational conditions on CO_2 plume size and pressure were presented based on extensive simulations runs and uncertainty analysis. The outcome of this study was also compared and found to be in good agreement with similar studies performed within the National Risk Assessment Partnership (NRAP) project. The National Risk Assessment Partnership (NRAP) project studied three distinct types of reservoirs, including an unbound, flat, single-layer sandstone, a domal, multi-layer sandstone with interbedded shale, and a domal, multi-layer limestone-dolostone (Kimberlina site in California [20], our study of the Citronelle reservoir, and the Rock Springs Uplift site [21] in Wyoming). Models for each of these reservoirs probed a common set of variables. In addition, each of the models explored some reservoir-specific variables (e.g., reservoir heterogeneity, tilt, etc.). Reservoir simulations were conducted at various injection rates and durations to probe the relationship between project size or reservoir conditions and risk. There were some differences in impacts of parameters between the domal structure vs. the larger, more open, systems. Two major observations were common among all the models obtained, including the plume behavior during injection that was predicted to be strongly tied to geological properties such as porosity, permeability, and reservoir lithology; and second, a related observation ties to the predicted behavior of reservoirs post injection.

Author Contributions: Conceptualization, E.F.; Methodology, E.F.; Validation, F.B.; Formal analysis, D.A.; Investigation, F.B.; Resources, F.B.; Data curation, D.A.; Writing—original draft, E.F.; Writing—review & editing, D.A. and F.B.; Visualization, D.A. All authors have read and agreed to the published version of the manuscript.

Funding: Work was funded by the US DOE-National Energy Technology Laboratory (Grant/Contract No. RES1000023 TRN 277) Develop Third-Generation ROMs for Reservoir Behavior (Activity No. 4000.2.651.072.002.242.000.005). We are also grateful to the research project CO2-Enhanced Oil Recovery for Carbon Capture Utilization and Storage (CCUS) in Colombia and Ecuador: A Norwegian Energy Initiative funded by the Norwegian Agency for Development and Cooperation (NORAD) under NORHED II 2021–2026. This project is carried out at the Escuela Superior Politécnica del Litoral (ESPOL) in the School of Engineering in Earth Sciences. Project number: FICT-300-2020.

Data Availability Statement: Data is available at https://edx.netl.doe.gov/dataset/?q=citronelle (accessed on 24 February 2023).

Conflicts of Interest: The authors declare no conflict of interest.

References

1. Kuuskraa, V.A.; Koperna, G.J.; Schepers, K. CO_2 Storage Engineering: Real Solution to Real Problems. Presented at the SPE International Conference on CO_2 Capture, Storage, and Utilization, New Orleans, LA, USA, 10–12 November 2010.
2. Bello, A.; Ivanova, A.; Cheremisin, A. A Comprehensive Review of the Role of CO_2 Foam EOR in the Reduction of Carbon Footprint in the Petroleum Industry. *Energies* **2023**, *16*, 1167. [CrossRef]
3. Ivanova, A.; Orekhov, A.; Markovic, S.; Iglauer, S.; Grishin, P.; Cheremisin, A. Live imaging of micro and macro wettability variations of carbonate oil reservoirs for enhanced oil recovery and CO2 trapping/storage. *Sci. Rep.* **2022**, *12*, 1262. [CrossRef] [PubMed]
4. Petrusak, R.; Cyphers, S.; Bumgardner, S.; Hills, D.; Pashin, J.; Esposito, R. Saline Reservoir Storage in an Active Oil Field: Extracting Maximum Value from Existing Data for Initial Site Characterization, Southeast Regional Carbon Sequestration Partnership (SECARB) Phase IIII Anthropogenic CO_2 Test at Citronelle Field. Presented at the SPE International Conference on CO_2 Capture, Storage, and Utilization, New Orleans, LA, USA, 10–12 November 2010.
5. Chen, S.E.; Liu, Y.; Peng, W. DoReMi-A Passive Geophysical Monitoring Technique for CO_2 Injection. Presented at the SPE Eastern Regional Meeting, Columbus, OH, USA, 17–19 August 2011. [CrossRef]
6. Kang, S.M.; Fathi, E.; Ambrose, R.J.; Akkutlu, I.Y.; Sigal, R.F. Carbon Dioxide Storage Capacity of Organic-Rich Shales. *SPE J.* **2011**, *16*, 842–855. [CrossRef]
7. Fathi, E.; Akkutlu, I.Y. Multi-component gas transport and adsorption effects during CO_2 injection and enhanced shale gas recovery. *Int. J. Coal Geol.* **2013**, *123*, 52–61. [CrossRef]
8. Fathi, E.; Akkutlu, I.Y. Counter-diffusion and Competitive Adsorption Effects during CO_2 Injection and Coalbed Methane Production. In Proceedings of the SPE Annual Technical Conference, Denver, CO, USA, 21–24 September 2008.
9. Esposito, R.; Rhudy, R.; Trautz, R.; Koperna, G.; Hill, G. Integrating carbon capture with transportation and storage. *Energy Procedia* **2011**, *4*, 5512–5519. [CrossRef]
10. Wang, H.; Kou, Z.; Ji, Z.; Wang, S.; Li, Y.; Jiao, Z.; Johnson, M.; McLaughlin, J.F. Investigation of enhanced CO_2 storage in deep saline aquifers by WAG and brine extraction in the Minnelusa sandstone, Wyoming. *Energy* **2023**, *265*, 126379. [CrossRef]
11. Qin, J.; Zhong, Q.; Tang, Y.; Rui, Z.; Qiu, S.; Chen, H. CO_2 storage potential assessment of offshore saline aquifers in China. *Fuel* **2023**, *341*, 127681. [CrossRef]
12. Barrufet, M.A.; Bacquet, A.; Gioia, F. Analysis of the Storage Capacity for CO_2 Sequestration of a Depleted Gas Condensate Reservoir and a Saline Aquifer. *J. Can. Pet. Technol.* **2010**, *49*, 23–31. [CrossRef]
13. Nghiem, L.; Shrivastava, V.; Kohse, B.; Hassam, M.; Yang, C. Simulation and Optimization of Trapping Processes for CO_2 Storage in Saline Aquifers. *J. Can. Pet. Technol.* **2010**, *49*, 15–22. [CrossRef]
14. Bennion, B.D.; Bachu, S. A Correlation of the Interfacial Tension between Supercritical Phase CO_2 and Equilibrium Brines as a Function of Salinity, Temperature and Pressure. Presented at the SPE (Society of Petroleum Engineers) Annual Technical Conference and Exhibition, Denver, CO, USA, 21–24 September 2008. [CrossRef]
15. Pashin, J.; McIntyre, M.; Grace, R.; Hills, D. *Southeastern Regional Carbon Sequestration Partnership (SECARB) Phase III, Final Report*; Advanced Resources International: Tuscaloosa, AL, USA, 2008.
16. Eaves, E. American Association of Petroleum Geologists. *Memoir* **1976**, *24*, 259–275.
17. Moreno, D. Comprehensive Analysis of an Ongoing CO_2 Storage Project. Master's Thesis, West Virginia University, Morgantown, WV, USA, 2013.
18. Koperna, G.J.; Riestenberg, D.E.; Kuuskraa, V.A.; Rhudy, R.; Trautz, R.C.; Hill, G.; Richard, A.E. The SECARB Anthropogenic Test: The First US Integrated Capture, Transportation, and Storage Test. Presented at the Carbon Management Technology Conference, Orlando, FL, USA, 7–9 February 2012. [CrossRef]
19. Zhang, X.; Ma, F.; Yin, S.; Wallace, C.D.; Soltanian, M.R.; Dai, Z.; Ritzi, R.W.; Ma, Z.; Zhan, C.; Lü, X. Application of upscaling methods for fluid flow and mass transport in multi-scale heterogeneous media: A critical review. *Appl. Energy* **2021**, *303*, 117603. [CrossRef]
20. Wainwright, H.; Finsterle, S.; Zhou, Q.; Birkholzer, J. *Modeling the Performance of Large-Scale CO_2 Storage Systems: A Comparison of Different Sensitivity Analysis Methods*; NRAPTRS-III-002-2012; NRAP Technical Report Series; U.S. Department of Energy; National Energy Technology Laboratory: Morgantown, WV, USA, 2012; p. 24.
21. Deng, H.; Stauffer, P.H.; Dai, Z.; Jiao, Z.; Surdam, R.C. Simulation of industrial-scale CO_2 storage: Multi-scale heterogeneity and its impacts on storage capacity, injectivity and leakage. *Int. J. Greenh. Gas Control* **2012**, *10*, 397–418. [CrossRef]